Advanced Powder Materials 2 (2023) 100133

Contents lists available at ScienceDirect

Advanced Powder Materials

journal homepage: www.keaipublishing.com/en/journals/advanced-powder-materials

An active and stable hydrogen electrode of solid oxide cells with exsolved Fe–Co–Ni nanoparticles from $Sr_2FeCo_{0.2}Ni_{0.2}Mo_{0.6}O_{6-\delta}$ double-perovskite

Cheng Li [a], Yatian Deng [a], Liping Yang [a], Bo Liu [a], Dong Yan [a], Liyuan Fan [b], Jian Li [a], Lichao Jia [a,*]

[a] School of Materials Science and Engineering, State Key Lab of Material Processing and Die & Mould Technology, Huazhong University of Science and Technology, Wuhan 430074, China

[b] College of Science and Engineering, James Cook University, 1 James Cook Drive, Townsville, QLD, 4811, Australia

ARTICLE INFO

Keywords:
Perovskite
Ternary alloy
Density functional theory
Solid oxide cells
Steam electrolysis

ABSTRACT

$Sr_2FeCo_{0.2}Ni_{0.2}Mo_{0.6}O_{6-\delta}$ (SFCNM) and $Sr_2FeNi_{0.4}Mo_{0.6}O_{6-\delta}$ (SFNM) were prepared as the hydrogen electrode materials for solid oxide cells (SOCs) and comparatively investigated by density function theory (DFT) and experiments to demonstrate the benefit of Co addition. The reduced SFCNM (R-SFCNM) and SFNM (R-SFNM) contain exsolved Fe–Co–Ni and Fe–Ni nanoparticles, respectively. DFT indicates that Fe–Co–Ni has optimized combination of the d-band center (descriptor of catalyst activity) and adsorption behavior for H_2O, H_2, H, and OH. The cell with SFCNM hydrogen electrode, $La_{0.8}Sr_{0.2}Ga_{0.8}Mg_{0.2}O_{3-\delta}$ (LSGM) electrolyte, and $La_{0.6}Sr_{0.4}Co_{0.2}Fe_{0.8}O_{3-\delta}$ (LSCF) oxygen electrode (Cell-SFCNM) demonstrates a higher performance than that with an SFNM hydrogen electrode (Cell-SFNM) at temperatures between 700 and 850 °C in both solid oxide fuel cell (SOFC, 3% H_2O-97% H_2/air) and solid oxide electrolysis cell (SOEC, 20% H_2O-80% H_2/air) modes. At 850 and 700 °C, the peak power density is 1.23 and 0.48 $W{\cdot}cm^{-2}$ in SOFC mode, while the current density is 1.25 and 0.37 $A{\cdot}cm^{-2}$ at 1.3 V in SOEC mode, respectively. The performance degradation rates at 750 °C are 0.17 $mV{\cdot}h^{-1}$ in SOFC and 0.15 $mV{\cdot}h^{-1}$ in SOEC modes within 150 h, which are improved by Co doping.

1. Introduction

Solid oxide cells (SOCs) are electrochemical energy conversion devices that can operate as power generation in solid oxide fuel cell (SOFC) mode and as energy storage (H_2O and CO_2 electrolysis) in solid oxide electrolysis cell (SOEC) mode at temperatures above 600 °C. They are high efficiency and environmentally friendly, thus have attracted extensive interest recently [1–5]. The SOC consists of three components, porous hydrogen electrode, dense electrolyte, and porous oxygen electrode. The basic requirements for the electrode materials are electrically and ionically conductive, electrochemically active, chemically stable, and thermally compatible with the electrolyte material [6,7].

The electrochemical function of the hydrogen electrode is to oxidize the fuel in SOFCs and reduce H_2O and CO_2 in conventional SOECs, therefore, its materials critically affect the performance of SOCs in both modes. In addition to costly noble metals, such as Pt [8], Ru [9], Pd [10], and Ir [11], Ni-based cermets are the state-of-the-art materials for the hydrogen electrodes, such as Ni–Y_2O_3 stabilized ZrO_2 (Ni-YSZ) and Ni–Gd-doped CeO_2 (Ni-GDC), and are widely utilized due to their excellent electrochemical activity and relatively low cost [12]. However, they suffer from Ni particle growth, migration, and oxidation in high H_2O atmospheres and carbon deposition when hydrocarbon fuels are used. These issues have limited the long-term applications of the Ni-based cermets in SOCs [13,14]. In recent years, a great deal of effort has been devoted to finding alternative materials to Ni-based cermets to solve these problems.

Perovskite materials (ABO_3) are promising due to their mixed ionic-electronic conductivity, such as $La_{0.8}Sr_{0.2}Cr_{0.5}Mn_{0.5}O_{3-\delta}$- [15,16], $La_{0.3}Sr_{0.7}TiO_{3-\delta}$- [17,18], and $La_xSr_{1-x}VO_{3-\delta}$-based [19,20] materials. However, their electronic [21] and ionic [22] conductivity and electrochemical activity [23,24] need to be further improved, and the difficulties in material preparation are to be overcome. Double perovskite (DP) $Sr_2Fe_{1.5}Mo_{0.5}O_{6-\delta}$ (SFM) contains Fe^{3+}/Fe^{2+} [25] and Mo^{6+}/Mo^{5+} ion pairs, exhibiting an adequate electronic conductivity in reducing atmosphere; its layered structure dictates a high oxygen vacancy concentration, in turn, an intrinsically high conductivity. Thus, it also can be used for the hydrogen electrode with its electrochemical activity improved [26,27] by either element doping or forming a composite with secondary phases [28–31]. Electrolyte material Sm-doped CeO_2 (SDC) was mixed with SFM, the SFM-SDC composite hydrogen electrode

* Corresponding author.
E-mail address: jialc@hust.edu.cn (L. Jia).

https://doi.org/10.1016/j.apmate.2023.100133
Received 4 February 2023; Received in revised form 6 April 2023; Accepted 6 April 2023
Available online 23 April 2023

demonstrated a better performance than single-phase SFM due to improved ionic conductivity by SDC [32]. Metal elements such as Ni [33,34], Co [35,36], and Ru [9] were doped into the B-site of SFM during material preparation. They exsolved from the lattice of SFM in a reducing atmosphere, forming metal alloy nanoparticles of Fe–Ni, Fe–Co, and Fe–Ru on the surface of the substrate with a layered Ruddlesden-Popper (RP) structure transformed from DP structure. The alloy nanoparticles, acting as an active component, improve the electrochemical performance and stability of the hydrogen electrodes due to the tight interfacial bonding between the particles and the substrate. Such an exsolution method was also used for preparing catalysts for CO_2 to formic acid conversion [37] and oxygen reduction in ionic liquids [38].

Fe–Co–Ni catalysts were reported to enhance the adsorption and desorption of the species involved in reactions and demonstrate improved catalytic activity for room temperature H_2O splitting [39], CH_4 dry reforming [40], and ethane dehydrogenation [41]. Stimulated by these findings, in the present study, the density function theory (DFT) was applied to predict the d-band center (a descriptor of catalyst activity) of Fe, Ni, and Co elements and alloys, as well as their adsorption ability of H_2O, OH, H, and H_2. Based on the DFT analysis, catalysts $Sr_2FeNi_{0.4}Mo_{0.6}O_{6-\delta}$ (SFNM) and $Sr_2FeCo_{0.2}Ni_{0.2}Mo_{0.6}O_{6-\delta}$ (SFCNM) were prepared and characterized alone and in-cell to demonstrate that Co addition improves the performance of SFNM for the hydrogen electrode of SOCs. As expected, the experimental results showed that Fe–Co–Ni ternary alloy nanoparticles were exsolved in a reducing atmosphere accompanied by a substrate transformation from the DP to RP structure. The composition of Fe–Co–Ni was precisely determined by STEM-EELS. And the enhanced electrochemical performance of the SFCNM hydrogen electrode was achieved over SFNM with exsolved Fe–Ni binary alloy nanoparticles for H_2 oxidation and H_2O electrolysis, which demonstrated that multi-alloying is an effective way to improve electrochemical performance.

2. Results and discussion

2.1. Theoretical prediction

The d-band center ε_d, i.e., the average energy of the d state of a metal atom, is a significant descriptor that is widely used to understand and evaluate the catalysis activity of the metal catalyst [42,43], including the adsorption and desorption activity of gases on the surface of catalyst [44–46]. We obtained the d-band centers of different metals firstly based on the calculated partial density of states (PDOS) to evaluate the catalysis activity of different metal nanoparticles (Fig. 1(a)). The values obtained for Fe, Co and Ni are −0.89, −0.91, and −1.10 eV, respectively, which are in good agreement with previous reports [47]. The smallest value of Ni (−1.1 eV) reveals the strongest binding activity between the catalyst and an intermediate that easily leads to surface poisoning; the too large value of Fe (−0.89 eV) indicates a limited availability of the catalytic activity. Thus, the modulating proportion of an alloy based on the above three metals can obtain a significant catalyst for adsorption. The values of bimetallic FeNi3 and trimetallic Fe2CoNi localize between the Co and Ni, which are −1.05 eV and −0.95 eV, respectively, exhibiting a suitable binding ability.

We further calculated the adsorption energies of two oxygen species (H_2O and OH) and the desorption energies of H_2 to evaluate the catalytic activity of catalysts in water decomposition. As shown in Fig. 1(b), trimetallic Fe2CoNi shows stronger adsorption ability for the two oxygen species than that of FeNi3 based on the smaller adsorption values of −0.477 eV to −0.433 eV for H_2O and −3.895 eV to −3.432 eV for OH; Fe2CoNi exhibits weaker adsorption ability for H_2 than FeNi3 because of the larger value of Fe2CoNi (0.059 eV) than that of FeNi3 (0.050 eV). These calculated values reveal the better catalytic performance of Fe2CoNi than that of FeNi3 in water decomposition.

2.2. Crystal structure and composition

Fig. 2 shows the crystal structure and composition of SFCNM, SFNM, Reduced-SFCNM (R-SFCNM), and Reduced-SFNM (R-SFNM) determined by X-ray diffraction, electron microscopy, and electron energy loss spectroscopy. It indicates that SFCNM and SFNM were single-phase with a DP structure, confirming that there was no $SrMoO_4$ phase formed in SFM-based DP with Mo content below 0.68 [48]. And R-SFCNM and R-SFNM consisted of two phases, i.e., a minor metallic phase containing either Fe, Co, and Ni or Fe and Ni, with a cubic structure and a major phase (substrate) with the RP structure transformed from DP structure (Fig. 2(a) and (b)) [33–36]. Due to Co addition partly replacing Ni in SFCNM, the diffraction pattern was left-shifted to smaller 2θ angles with respect to that of SFNM (insert in Fig. 2(a)), indicating a lattice expansion as Co^{2+} (0.075 nm) is larger than Ni^{2+} (0.069 nm). The results of Rietveld refinement showed that SFCNM and SFNM, the substrates, and the metallic phases possessed a symmetry of I4/m, I4/mmm, and Pm-3m, respectively (Fig. S6 and Table S2), and the weight ratio of the metallic phase to the substrate was estimated about 11.3–88.7 and 10.7 to 89.3, respectively, in R-SFCNM and R-SFNM (Table S3). The symmetry of SFCNM and R-SFCNM was further confirmed as above by a high-resolution transmission electron microscope (HR-TEM) based on the interplanar spacing of corresponding lattice plans, such as 0.394 and 0.396 nm for (110) and (002) planes of SFCNM, 0.205 nm for (111) plane of the metallic nanoparticles, and 0.284 nm for (015) plane of the transformed substrate (Fig. 2(c) and (d)).

The composition of the exsolved metallic phase and the substrate of R-SFCNM was estimated by electronic energy-loss spectroscopy (EELS, Fig. 2(e) and (f)). Areas 1 and 2 were regions of different metallic

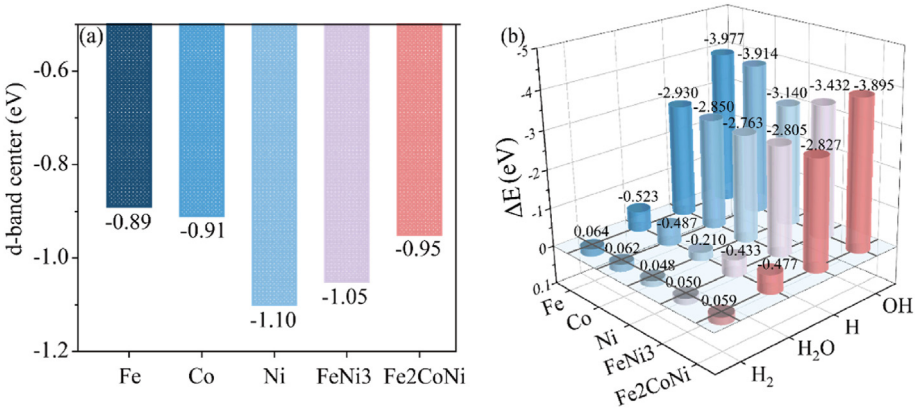

Fig. 1. DFT calculations for Fe, Co, and Ni and their alloys (original calculated results inFig. S5 and Table S1): (a) d-band center ε_d and (b) binding energies of the hydrogen species absorbed on (111) surfaces of different catalysts.

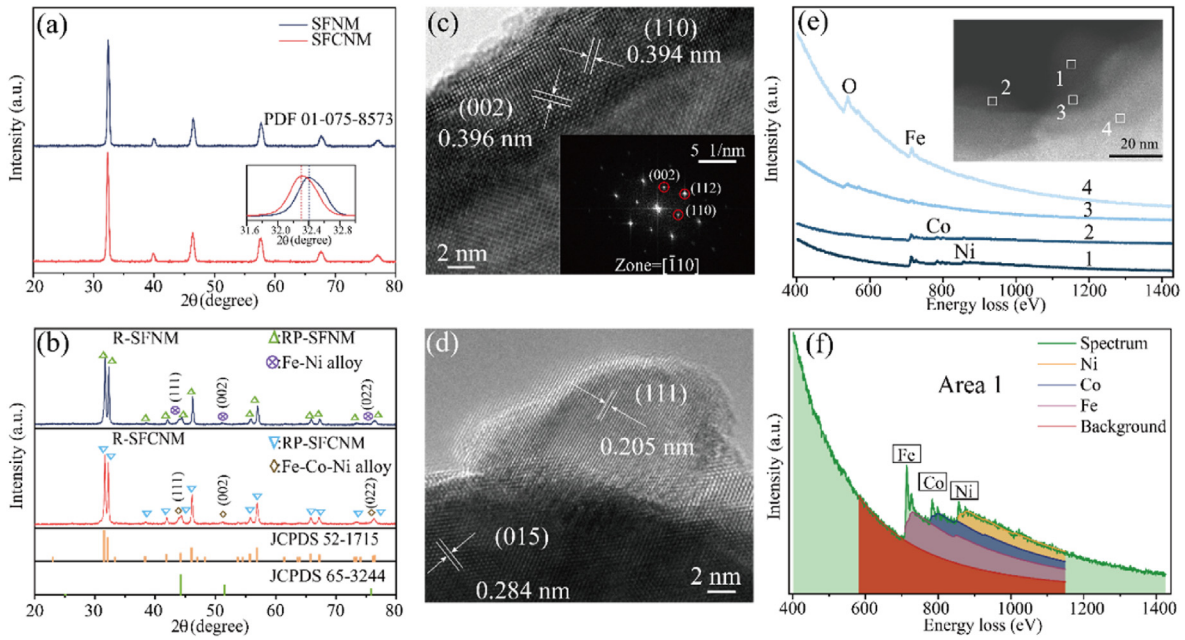

Fig. 2. Crystal structure, microstructure, and composition: XRD spectra of (a) SFCNM and SFNM and (b) R-SFCNM and R-SFNM; High-resolution images of (c) SFCNM and (d) R-SFCNM; (e) STEM-EELS spectra and dark field-STEM image of R-SFCNM; (f) Alloy composition calculation of area 1 in (e).

nanoparticles, and areas 3 and 4 were two regions of the substrate. The EELS spectra from these areas showed peaks at various values of energy that corresponded to the characteristic energy of electrons in different elements. It is well known that the peaks at 532, 708, 779, and 855 eV (Fig. 2(e)) are related to the electron energy states of O K, Fe L, Co L, and Ni L, respectively [49–51]. Thus, it can be determined that the exsolved metallic nanoparticles contained only Fe, Co, and Ni elements, and an undetectable amount of Co and Ni remained in the substrate as the reducibility follows the order of Ni > Co > Fe [52]. With the result shown in Fig. 2(e), the atomic ratio of Fe, Co, and Ni in nanoparticles 1 and 2

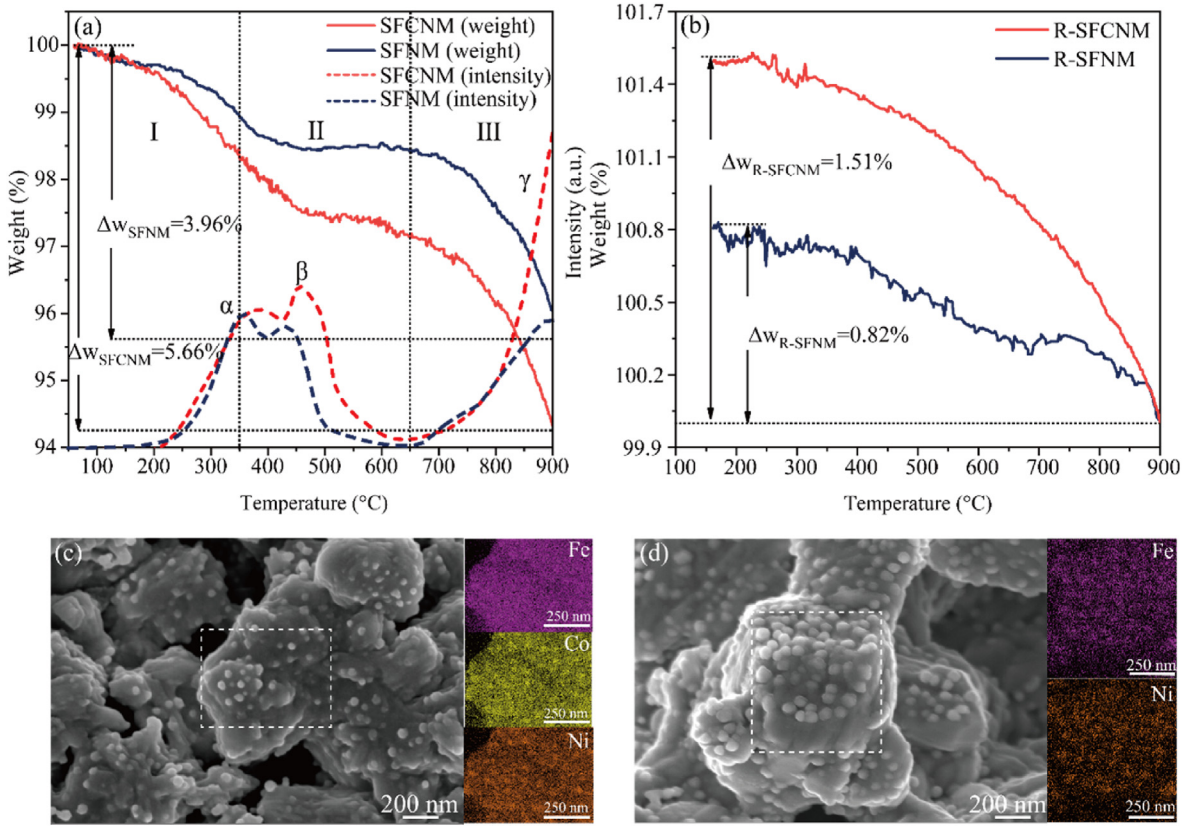

Fig. 3. Reduction, water adsorption, and morphology: (a) H_2-TPR profile and weight loss of SFCNM and SFNM in 5% H_2–N_2; (b) Water absorption of R-SFCNM and R-SFNM in 5% H_2O-Ar at 20 ml·min^{-1} and 10 °C·min^{-1}; Morphologies and element distributions of (c) R-SFCNM and (d) R-SFNM.

was determined as 44.2:24.9:30.9, 45.5:24.0:30.5, with an average of about 45:25:30 (Fig. 2(f)). According to the composition of exsolved Fe–Co–Ni metallic phase, it is expected that the following reactions occurred during the reduction of SFCNM in H_2:

$$3Sr_2FeCo_{0.2}Ni_{0.2}Mo_{0.6}O_{6-\delta} + nH_2 \rightarrow 2Sr_3Fe_{1.05}Co_{0.05}Mo_{0.9}O_{7-\delta} + 2Fe_{0.45}Co_{0.25}Ni_{0.3} + nH_2O + nV_{\ddot{O}} \quad (1)$$

accompanied by the formation of oxygen vacancies ($V_{\ddot{O}}$) that promotes surface oxygen exchange and diffusion and in turn electrocatalytic activity of R-SFCNM.

2.3. Reduction/water absorption behaviors and morphology

Reduction thermogravimetric analysis (TGA) and H_2-temperature programmed reduction (H_2-TPR) were carried from room temperature to 900 °C in 5% H_2–N_2 for SFCNM and SFNM, respectively, followed by water adsorption in 5% H_2O–Ar from 900 °C to 50 °C. The weight change of the specimens during these processes was recorded as shown in Fig. 3. During reduction TGA, the weight loss (Fig. 3(a)), caused by either desorption of adsorbed H_2O and other species or release of lattice oxygen, can be divided into three stages, i.e., stage I (200–350 °C), II (350–650 °C), and III (650–900 °C) corresponding to the profile of H_2-TPR shown in dotted lines. H_2 was consumed to reduce the metallic ions from their high to low valences accompanied with oxygen release, such as Fe^{3+} to Fe^{2+} at ~357 °C (α peak), Mo^{6+} to Mo^{5+} at ~430 °C (β peak), and Fe^0, Ni^0, and Co^0 were formed in alloys above 700 °C (γ peak) [34, 53–55] as detected by X-ray photoelectron spectroscopy (XPS, Fig. S7). And meanwhile, the substrate was transformed from DP to RP structure [56], as shown by the high-temperature XRD patterns (Fig. S8), with much more oxygen vacancies for adsorbing oxygen species such as $O_{ad.}$ and H_2O_{ad} (Fig. S7(e) and Table S4) to facilitate surface reactions [57, 58]. Co addition made the H_2-TPR profile right shifting to higher temperatures, suggesting that SFNM is more reducible than SFCNM. The higher concentration of oxygen vacancy in R-SFCNM explains that it adsorbed more H_2O (1.51%) than R-SFNM (0.82%) during cooling from 900 °C in 5% H_2O–Ar atmosphere (Fig. 3(b)), and a promoted H_2O electrolysis performance is expected with R-SFCNM, as the adsorbed H_2O is the reactant needed for the reactions. Before the reduction, SFCNM and SFNM were single-phase materials with smooth surfaces (Fig. S9); after that, exsolved metallic nanoparticles were formed and tightly distributed on the substrate with an average size of 32 and 48 nm for Fe–Co–Ni in R-SFCNM and Fe–Ni in R-SFNM, respectively (Fig. 3(c) and (d), Fig. S10). The smaller size of Fe–Co–Ni nanoparticles also indicates that SFCNM is less reducible than SFNM.

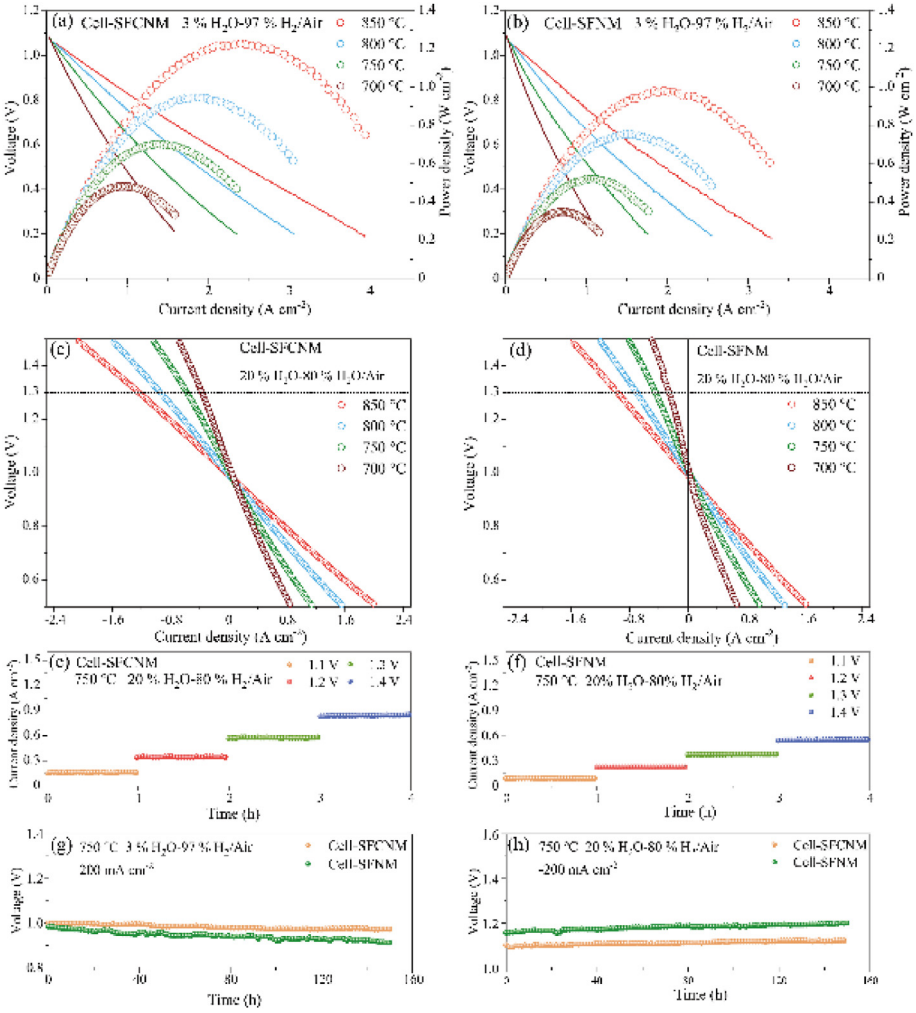

Fig. 4. Electrochemical performance of Cell-SFCNM and Cell-SFNM in both SOFC and SOEC modes: I–V–P curves in SOFC mode of (a) Cell-SFCNM and (b) Cell-SFNM; I–V responses in SOEC mode of (c) Cell-SFCNM and (d) Cell-SFNM; Short-term performance in SOEC mode of (e) Cell-SFCNM and (f) Cell-SFNM; Long-term stability of Cell-SFCNM and Cell-SFNM in (g) SOFC and (h) SOEC modes.

2.4. Electrochemical performance

2.4.1. Short- and long-term performance

For comparison, cells were prepared with SFCNM-$Gd_{0.1}Ce_{0.9}O_{2-\delta}$ (GDC) and SFNM-GDC hydrogen electrodes, named Cell-SFCNM and Cell-SFNM, respectively. Fig. 4 shows the electrochemical performance of Cell-SFCNM and Cell-SFNM in both SOFC and SOEC modes. With 3% H_2O-97% H_2 as fuel and air as oxidant under SOFC conditions (Fig. 4(a) and (b)), the open circuit voltages (OCV) of the cells ranged from 1.058 to 1.092 V at temperatures between 850 °C and 700 °C. They are close to that predicted by the Nernst equation, suggesting that the cells were free of pinholes across the electrolyte and well-sealed during the test. The peak power density of Cell-SFCNM (1.23, 0.95, 0.70, and 0.48 W·cm^{-2} at 850, 800, 750, and 700 °C, respectively) was higher than that of Cell-SFNM (0.99, 0.75, 0.52, and 0.35 W·cm^{-2} at 850, 800, 750, and 700 °C, respectively). In SOEC mode with 20% H_2O-80% H_2 in the hydrogen electrode and air in the oxygen electrode (Fig. 4(c) and (d)), the OCV (from 0.994 V to 1.027 V) was lower, compared to that in SOFC mode, due to a higher concentration of water vapor. The current density at the thermoneutral voltage of 1.3 V was −1.25, −0.94, −0.58, and −0.37 A·cm^{-2} at 850, 800, 750, and 700 °C, respectively, for Cell-SFCNM, which is higher than that of Cell-SFNM (−0.98, −0.71, −0.45, and −0.26 A·cm^{-2} at 850, 800, 750, and 700 °C, respectively).

To obtain an overall understanding of SFCNM and SFNM electrodes in SOEC mode, Cell-SFCNM and Cell-SFNM were evaluated with 20% H_2O-80% H_2 and air at 750 °C and various applied voltages between 1.1 and 1.4 for a short period of 1 h. The performance of both cells was stable within 1 h; however, the current density of Cell-SFCNM (Fig. 4(e)) was higher than that of Cell-SFNM (Fig. 4(f)), suggesting that SFCNM outperformed SFNM as demonstrated by the I–V curves (Fig. 4(c) to 4(d)). According to that, these two cells were further tested for a longer time of 150 h at 750 °C and constant current density in both SOFC (200 mA·cm^{-2}, 3% H_2O-97% H_2/air) and SOEC (−200 mA·cm^{-2}, 20% H_2O-80% H_2/air) modes (Fig. 4(g) and (h)). The voltage of the cells decreased with time in SOFC mode, 0.17 mV h^{-1} for Cell-SFCNM and 0.50 mV·h^{-1} Cell-SFNM; while increased in SOEC mode, 0.15 and 0.27 mV·h^{-1} for Cell-SFCNM and Cell-SFNM, respectively. These results indicate again that the Co and Ni co-doped SFCNM is more electrochemically active and stable than the Ni-doped SFNM, the reason for which was further explored by following EIS (electrochemical impedance spectra) and DRT (distribution of relaxation time) analysis. Nevertheless, the electrochemical performance of the cells in the present study is comparable with and even better than the results reported in the literature (Tables S5 and S6).

2.4.2. EIS and DRT analysis

Fig. 5 shows the EIS at OCV of Cell-SFCNM and Cell-SFNM under the conditions of SOFC and SOEC modes at various temperatures and the derived DRT. Both the cells demonstrated similar ohmic resistance, mainly contributed by the $La_{0.8}Sr_{0.2}Ga_{0.8}Mg_{0.2}O_{3-\delta}$ (LSGM) electrolyte and $La_{0.4}Ce_{0.6}O_{2-\delta}$ (LDC) buffer layer, therefore, it was the difference in their electrode polarization resistance (R_p) that led to the difference in their performance. In SOFC mode (3% H_2O-97% H_2/air), the R_p of Cell-SFCNM was between 0.095 and 0.385 Ω·cm^2 at temperatures from 850 to 700 °C, lower than that of Cell-SFNM in the same temperature range, from 0.11 at 850 °C to 0.64 Ω·cm^2 at 700 °C (Fig. 5(a)). In SOEC mode (20% H_2O-80% H_2), the R_p of Cell-SFCNM (from 0.06 Ω·cm^2 at 850 °C to 0.31 Ω·cm^2 at 700 °C) was also smaller than that of Cell-SFNM (from 0.09 Ω·cm^2 at 850 °C to 0.61 Ω·cm^2 at 700 °C) (Fig. 5(b)), and the R_p of both the cells at 1.3 V was smaller than that at OCV (Fig. S11), suggesting that applied boosts the electrode reactions of H_2O electrolysis.

According to the EIS, the DRT at 750 °C in both SOFC and SOEC modes was obtained (Fig. 5(c) and (d)) using the DRTtools software [59,60] with a regularization factor of 10^{-3}, showing four characteristic peaks of P1 to P4 corresponding the processes occurring on the electrodes. The high-frequency P1 represents charge-transfer processes in the electrodes, the mid-frequency P2 corresponds to electrode surface processes involving gas adsorption and desorption and electrochemical reactions, P3 in the low-medium frequency range is contributed by gas diffusion in electrodes, and the low-frequency P4 is caused by gas conversion (like gas dissociation and activation) on hydrogen electrode [54,61–65]. The areas underneath all the peaks were smaller for Cell-SFCNM than for Cell-SFNM, except that below P1 (Table S7), which suggests that Fe–Co–Ni particle exsolution promoted all the processes occurring in the SFCNM hydrogen electrode but that of the charge transfer. The reason is that Fe–Co–Ni particles have higher catalytic activity, and the RP-SFCNM support has a higher oxygen vacancy

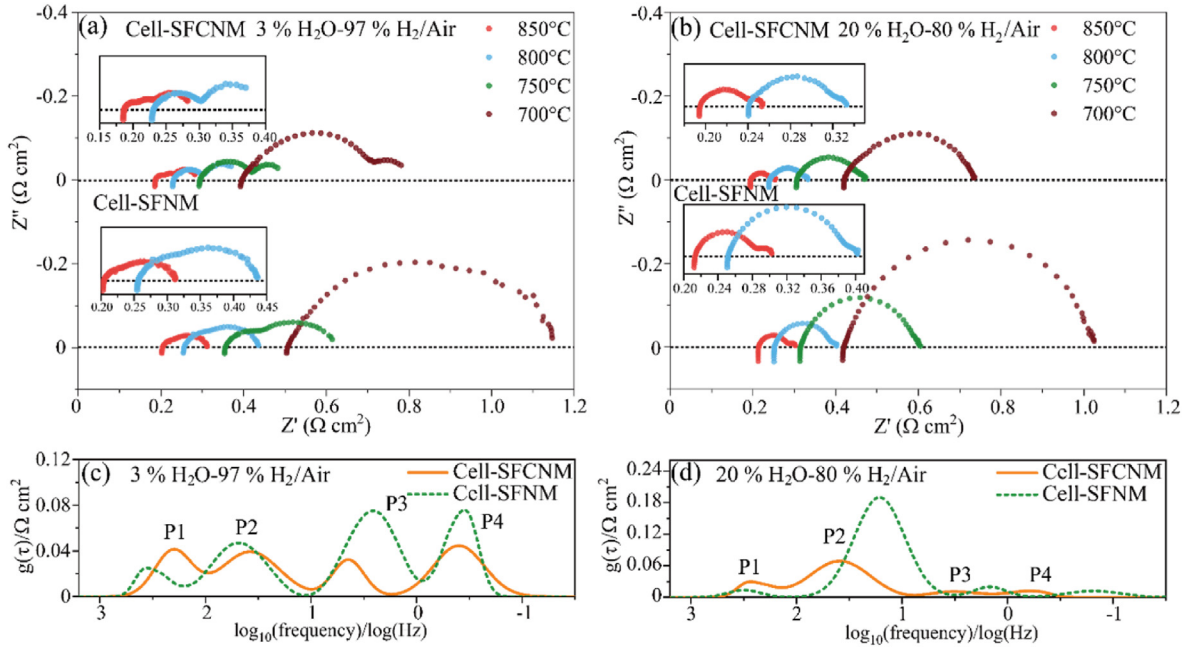

Fig. 5. EIS (OCV and 750 °C) and derived DRT of Cell-SFCNM and Cell-SFNM in both SOFC and SOEC modes: EIS of Cell-SFCNM and Cell-SFNM in (a) SOFC and (b) SOEC modes; DRT of Cell-SFCNM and Cell-SFNM in (c) SOFC and (d) SOEC modes.

concentration for H_2 and H_2O adsorption and dissociation, and H and OH surface diffusion. And the slight increase in charge transfer polarization of SFCNM may be caused by the larger lattice distortion of Fe–Co–Ni than Fe–Ni particles. Furthermore, as mentioned above, the weight ratio of exsolved nanoparticles to the substrate in R-SFCNM is higher than that in R-SFNM, and the particle sizes of Fe–Co–Ni are smaller than Fe–Ni. The smaller exsolved nanoparticles may indicate the stronger connection with the substrate, better dispersion and larger surface areas/active sites, which results in better and more stable electrochemical performance [66–69]. However, the deeper origin for the improved electrochemical performance caused by particles' morphology like size still needs further investigation.

3. Conclusion

$Sr_2FeCo_{0.2}Ni_{0.2}Mo_{0.6}O_{6-\delta}$ (SFCNM) and $Sr_2FeNi_{0.4}Mo_{0.6}O_{6-\delta}$ (SFNM) were comparatively investigated as the hydrogen electrode materials for SOCs to demonstrate the contribution of Co addition to the electrode performance. Based on the theoretical and experimental results, the following conclusions are drawn.

(1) Co has a d-band center (ε_d) between that of Fe and Ni, its addition into Fe–Ni alloy renders an optimized combination of ε_d and the adsorption energy (ΔE) of H_2O, H_2, H, and OH, enhancing the activity for electrolysis.
(2) After the reduction in H_2, nanoparticles of Fe–Ni and Fe–Co–Ni are exsolved in SFCNM and SFNM, respectively, with the substrate crystal structure transformed from DP to RP structure with increased oxygen vacancies and more H_2O adsorption of R-SFCNM than R-SFNM.

The electrochemical performance and stability of Cell-SFCNM are improved in both SOFC and SOEC modes, compared to Cell-SFNM, due to that Fe–Co–Ni nanoparticles in RP-SFCNM have higher catalytic activity, and the substrate has more oxygen vacancies for H_2 and H_2O adsorption and dissociation, and H and OH diffusion.

4. Theoretical and experimental

4.1. DFT calculation

DFT calculations were performed using the Vienna ab-initio Simulation Package (VASP) with plane-wave-based projector augmented-wave pseudopotentials [70]. The generalized gradient approximation (GGA) in the form of the Perdew-Burke-Ernzerhof (PBE) functional was utilized to evaluate the electron exchange and correlation effects [71]. FeNi3 (111) and Fe2CoNi (111) surfaces were modeled by a four-layer plate of (2 × 2) supercell with a vacuum thickness of 15 Å, a Monkhorst-Pack k-point grid of 2 × 2× 1, and an energy cutoff of 300 eV. The structure was fully optimized until the Hellmann Feynman force was smaller than 0.02 eV·Å^{-1} and the energy below 1 × 10^{-5} eV.

FeNi3 (111) and Fe2CoNi (111) surfaces were modeled by a four-layer plate of (2 × 2) supercell with a vacuum thickness of 15 Å, a Monkhorst-Pack k-point grid of 2 × 2× 1, and an energy cutoff of 300 eV. The structure was fully optimized until the Hellmann Feynman force was smaller than 0.02 eV·Å^{-1} and the energy below 1 × 10^{-5} eV. The structures used in this study were presented in Figs. S1–S4.

The energy (ΔE) of adsorption or desorption was calculated using the equation:

$$\Delta E = E_{tot} - \left(E_{surf} + E_{adsorbate}\right) \quad (2)$$

where E_{tot} is the total energy of the adsorbed assembly, E_{surf} is the energy of the surface structure of catalyst, and $E_{adsorbate}$ is the energy of adsorbate. A negative value reveals the adsorption process while a positive value indicates the desorption process.

The d-band center (ε_d) of metal is calculated based on the calculated density of states (DOS) by the equation:

$$\varepsilon_d = \frac{\int_{-\infty}^{+\infty} n_d(\varepsilon)\varepsilon d\varepsilon}{\int_{-\infty}^{+\infty} n_d(\varepsilon) d\varepsilon} \quad (3)$$

where n_d is the DOS of metal-d state and ε is the energy of the corresponding state.

4.2. Materials preparation

SFCNM powder was prepared by a solution method. Firstly, stoichiometric amounts of $Sr(NO_3)_2$, $Fe(NO_3)_3{\cdot}9H_2O$, $Co(NO_3)_2{\cdot}6H_2O$, $Ni(NO_3)_2{\cdot}6H_2O$, and $(NH_4)_6Mo_7O_{24}{\cdot}4H_2O$ (purity >98%, Aladdin, Inc.) were dissolved in deionized water, followed by adding glycine and citric acid to form a clear solution. The molar ratio of total metallic ions, citric acid, and glycine was about 1:1.5:2. This solution was held at 80 °C under agitation for 4 h to evaporate the solvent and then at ~600 °C for 30 min to form an aerogel, which was calcined at 1100 °C in the air for 6 h to form SFCNM powder. The powders of SFNM, $La_{0.6}Sr_{0.4}Co_{0.2}Fe_{0.8}O_{3-\delta}$ (LSCF) for the oxygen electrode, and LDC for the buffer layer were synthesized similarly. Some SFCNM and SFNM powders were reduced in H_2 at 850 °C for 2 h, designated as R-SFCNM and R-SFNM.

4.3. Materials characterization

H_2-TPR (TP-5080) was carried out up to 900 °C at 5 °C·min^{-1} for SFCNM and SFNM in 5% H_2–N_2 atmosphere at 20 ml min^{-1}, and the weight change of the specimens upon the reduction was monitored by a thermogravimetric analyzer (TGA, STA 449F5, Netzsch). R-SFCNM and R-SFNM were subjected to thermogravimetric analysis from 900 °C to 50 °C in 5% H_2O–Ar atmosphere.

The crystal structure of the as-prepared and reduced SFCNM and SFNM was examined using XRD (Panalytical X'Pert) with Cu K_α radiation (λ=1.5418 Å) at 40 kV and 40 mA. The scanning covered a 2θ range from 20° to 80° with a step of 0.02° at 10° min^{-1}. The diffraction data were refined by the Rietveld method using the GSAS program. The lattice images of SFCNM and R-SFCNM were obtained by a HR-TEM (FEI Tecnai F20), and the morphology and element distribution were examined by a scanning electron microscope attached with an energy dispersive X-ray spectrometer (SEM, Sirion200). And the composition of Fe–Co–Ni nanoparticles was verified by scanning transmission electro-microscopy (STEM, Thermo Fisher Titan Themis G2 60–300) and its EELS. XPS (Thermo Scientific K-Alpha) was conducted to analyze the valence of the surface elements of SFCNM, SFNM, R-SFCNM, and R-SFNM by the Avantage software.

4.4. Cell preparation

The cell structure was electrolyte-supported with LSGM (Fuel Cell Materials, Inc.) electrolyte. The cell configuration was hydrogen electrode/buffer layer/electrolyte/oxygen electrode. For comparison, cells were prepared with SFCNM- GDC (Sofcman, Inc.) and SFNM-GDC hydrogen electrodes, named Cell-SFCNM and Cell-SFNM, respectively. LDC was used for the buffer layer to prevent the reactions between the hydrogen electrode and electrolyte, and the composite LSCF-GDC was employed for the oxygen electrode. The cell support of the LSGM electrolyte was prepared by dry pressing LSGM powder mixed with a certain amount of PVB-98 binder under 10 MPa for 1 min in a 15 mm-diameter mold and sintering at 1400 °C in the air for 4 h. It was then polished to a thickness of around 270 μm. The buffer layer, around 10 μm thick, was prepared by printing an LDC slurry containing 2.5 g LDC, 0.05 g triethanolamine, 0.05 g dibutyl phthalate, 0.05 g PVB-98, and 11.9 g ethanol onto one side of the LSGM electrolyte support and sintering at 1300 °C for 2 h. The hydrogen electrode was printed onto the LDC buffer layer

with a slurry containing 25 wt% SFCNM, 25 wt% GDC, 5 wt% toner, and 45 wt% terpineol containing 4 wt% ethyl cellulose. Similarly, the oxygen electrode was printed on the other surface of LSGM symmetrically opposite to the hydrogen electrode with a slurry containing 70 wt% LSCF and 30 wt% GDC. The printed hydrogen and oxygen electrodes were co-sintered at 1050 °C in the air for 2 h, and the thickness of electrodes was 15–25 μm with an effective area of ~0.28 cm^{-2}. Pt slurry was then coated on the electrodes and baked at 850 °C in the air for 2 h to serve as the current collectors. Cell-SFNM was also prepared likewise.

4.5. Cell evaluation

Before testing, the SFCNM-GDC and SFNM-GDC hydrogen electrodes were reduced at 850 °C for 2 h with humid H_2 (3% H_2O) flowing into the hydrogen electrode and air into the oxygen electrode at 30 ml min^{-1}. During the test in SOFC mode, the atmosphere in the hydrogen and oxygen electrodes remained the same as above; 20% H_2O-80% H_2 was used as fuel in SOEC mode. The current (I)-voltage (V) curves and EIS (frequency 10^6 to 10^{-1} Hz, bias voltage 10 mV) were obtained at temperatures from 700 °C to 850 °C using an electrochemical workstation consisting of Solartron 1287 and 1260A. And performance stability at 750 °C was also evaluated.

Declaration of competing interest

The authors declare that they have no known competing financial interests or personal relationships that could have appeared to influence the work reported in this paper.

Acknowledgement

This research was financially supported by the National Natural Science Foundation of China (52072134, U1910209, 51972128, 52272205), and Hubei Province (2021CBA149, 2021CFA072, 2022BAA087). The XRD, TEM, and XPS characterizations were assisted by the Analytical and Testing Center of Huazhong University of Science and Technology.

Appendix A. Supplementary data

Supplementary data to this article can be found online at https://doi.org/10.1016/j.apmate.2023.100133.

References

[1] A. Hauch, R. Küngas, P. Blennow, A.B. Hansen, J.B. Hansen, B.V. Mathiesen, M.B. Mogensen, Recent advances in solid oxide cell technology for electrolysis, Science 370 (2020), eaba6118.
[2] M.A. Alkhadra, X. Su, M.E. Suss, H. Tian, E.N. Guyes, A.N. Shocron, K.M. Conforti, J.P. de Souza, N. Kim, M. Tedesco, K. Khoiruddin, I.G. Wenten, J.G. Santiago, T.A. Hatton, M.Z. Bazant, Electrochemical methods for water purification, ion separations, and energy conversion, Chem. Rev. 122 (16) (2022) 13547–13635.
[3] R. Ren, X. Yu, Z. Wang, C. Xu, T. Song, W. Sun, J. Qiao, K. Sun, Fluorination inductive effect enables rapid bulk proton diffusion in $BaCo_{0.4}Fe_{0.4}Zr_{0.1}Y_{0.1}O_{3-\delta}$ perovskite oxide for high-activity protonic ceramic fuel cell cathode, Appl. Catal., B 317 (2022), 121759.
[4] D. Zhang, Y. Chen, H. Vega, T. Feng, D. Yu, M. Everett, J. Neuefeind, K. An, R. Chen, J. Luo, Long- and short-range orders in 10-component compositionally complex ceramics, Adv. Powder Mater. 2 (2) (2023), 100098.
[5] Q. Wang, X. Tong, S. Ricote, R. Sažinas, P.V. Hendriksen, M. Chen, Nano-$LaCoO_3$ infiltrated $BaZr_{0.8}Y_{0.2}O_3$− electrodes for steam splitting in protonic ceramic electrolysis cells, Adv. Powder Mater. 1 (1) (2022), 100003.
[6] P. Boldrin, N.P. Brandon, Progress and outlook for solid oxide fuel cells for transportation applications, Nat. Catal. 2 (7) (2019) 571–577.
[7] R. Wang, L.R. Parent, S. Gopalan, Y. Zhong, Experimental and computational investigations on the SO_2 poisoning of $(La_{0.8}Sr_{0.2})_{0.95}MnO_3$ cathode materials, Adv. Powder Mater. 2 (1) (2023), 100062.
[8] K. Kerman, B.K. Lai, S. Ramanathan, Pt/$Y_{0.16}Zr_{0.84}O_{1.92}$/Pt thin film solid oxide fuel cells: Electrode microstructure and stability considerations, J. Power Sources 196 (5) (2011) 2608–2614.
[9] H. Lv, L. Lin, X. Zhang, R. Li, Y. Song, H. Matsumoto, N. Ta, C. Zeng, Q. Fu, G. Wang, X. Bao, Promoting exsolution of RuFe alloy nanoparticles on $Sr_2Fe_{1.4}Ru_{0.1}Mo_{0.5}O_{6-\delta}$ via repeated redox manipulations for CO_2 electrolysis, Nat. Commun. 12 (1) (2021) 5665.
[10] R. Fu, P. Jiang, H. Xu, B. Niu, F. Jiang, L. Yang, T. Feng, T. He, Performance of Pd-impregnated $Sr_{1.9}FeNb_{0.9}Mo_{0.1}O_{6-\delta}$ double perovskites as symmetrical electrodes for direct hydrocarbon solid oxide fuel cells, Int. J. Hydrogen Energy 44 (59) (2019) 31394–31405.
[11] Z. Bian, S. Das, M.H. Wai, P. Hongmanorom, S. Kawi, A review on bimetallic nickel-based catalysts for CO_2 reforming of methane, ChemPhysChem 18 (22) (2017) 3117–3134.
[12] L. Ye, K. Xie, High-temperature electrocatalysis and key materials in solid oxide electrolysis cells, J. Energy Chem. 54 (2021) 736–745.
[13] G. Tsekouras, D. Neagu, J.T.S. Irvine, Step-change in high temperature steam electrolysis performance of perovskite oxide cathodes with exsolution of B-site dopants, Energy Environ. Sci. 6 (1) (2013) 256–266.
[14] S.D. Kim, D.W. Seo, A.K. Dorai, S.K. Woo, The effect of gas compositions on the performance and durability of solid oxide electrolysis cells, Int. J. Hydrogen Energy 38 (16) (2013) 6569–6576.
[15] R. Xing, Y. Wang, Y. Zhu, S. Liu, C. Jin, Co-electrolysis of steam and CO_2 in a solid oxide electrolysis cell with $La_{0.75}Sr_{0.25}Cr_{0.5}Mn_{0.5}O_{3-\delta}$–Cu ceramic composite electrode, J. Power Sources 274 (2015) 260–264.
[16] S. Zhang, Y. Wan, Z. Xu, S. Xue, L. Zhang, B. Zhang, C. Xia, Bismuth doped $La_{0.75}Sr_{0.25}Cr_{0.5}Mn_{0.5}O_{3-\delta}$ perovskite as a novel redox-stable efficient anode for solid oxide fuel cells, J. Mater. Chem. 8 (23) (2020) 11553–11563.
[17] S.H. Cui, J.H. Li, X.W. Zhou, G.Y. Wang, J.L. Luo, K.T. Chuang, Y. Bai, L.J. Qiao, Cobalt doped $LaSrTiO_{3-\delta}$ as an anode catalyst: Effect of Co nanoparticle precipitation on SOFCs operating on H_2S-containing hydrogen, J. Mater. Chem. 1 (34) (2013) 9689–9696.
[18] J.H. Myung, D. Neagu, D.N. Miller, J.T. Irvine, Switching on electrocatalytic activity in solid oxide cells, Nature 537 (7621) (2016) 528–531.
[19] J.-S. Park, I.D. Hasson, M.D. Gross, C. Chen, J.M. Vohs, R.J. Gorte, A high-performance solid oxide fuel cell anode based on lanthanum strontium vanadate, J. Power Sources 196 (18) (2011) 7488–7494.
[20] Y. Li, G. Wu, C. Ruan, Q. Zhou, Y. Wang, W. Doherty, K. Xie, Y. Wu, Composite cathode based on doped vanadate enhanced with loaded metal nanoparticles for steam electrolysis, J. Power Sources 253 (2014) 349–359.
[21] S. Plint, P. Connor, S. Tao, J. Irvine, Electronic transport in the novel SOFC anode material $La_{1-x}Sr_xCr_{0.5}Mn_{0.5}O_{3\pm\delta}$, Solid State Ionics 177 (19–25) (2006) 2005–2008.
[22] M. Wu, X. Zhou, J. Xu, S. Li, L. Pan, N. Zhang, Electrochemical performance of $La_{0.3}Sr_{0.7}Ti_{0.3}Fe_{0.7}O_{3-\delta}$/$CeO_2$ composite cathode for CO_2 reduction in solid oxide electrolysis cells, J. Power Sources 451 (2020), 227334.
[23] X. Zhang, Y. Song, F. Guan, Y. Zhou, H. Lv, Q. Liu, G. Wang, X. Bao, $La_{0.75}Sr_{0.25})_{0.95}(Cr_{0.5}Mn_{0.5})O_{3-\delta}$-$Ce_{0.8}Gd_{0.2}O_{1.9}$ scaffolded composite cathode for high temperature CO_2 electroreduction in solid oxide electrolysis cell, J. Power Sources 400 (2018) 104–113.
[24] S. Primdahl, J.R. Hansen, L. Grahl-Madsen, P.H. Larsen, Sr-doped $LaCrO_3$ anode for solid oxide fuel cells, J. Electrochem. Soc. 148 (1) (2001) A74–A81.
[25] R. Ren, J. Sun, G. Wang, C. Xu, J. Qiao, W. Sun, Z. Wang, K. Sun, Rational design of $Sr_2Fe_{1.5}Mo_{0.4}Y_{0.1}O_{6-\delta}$ oxygen electrode with triple conduction for hydrogen production in protonic ceramic electrolysis cell, Sep. Purif. Technol. 299 (2022), 121780.
[26] P. Qiu, S. Sun, J. Li, L. Jia, A review on the application of $Sr_2Fe_{1.5}Mo_{0.5}O_6$-based oxides in solid oxide electrochemical cells, Sep. Purif. Technol. 298 (2022), 121581.
[27] P. Qiu, J. Lin, L. Lei, Z. Yuan, L. Jia, J. Li, F. Chen, Evaluation of Cr-tolerance of the $Sr_2Fe_{1.5}Mo_{0.5}O_{6-\delta}$ cathode for solid oxide fuel cells, ACS Appl. Energy Mater. 2 (10) (2019) 7619–7627.
[28] S. Vasala, M. Lehtimäki, Y.H. Huang, H. Yamauchi, J.B. Goodenough, M. Karppinen, Degree of order and redox balance in B-site ordered double-perovskite oxides, $Sr_2MMoO_{6-\delta}$ (M=Mg, Mn, Fe, Co, Ni, Zn), J. Solid State Chem. 183 (5) (2010) 1007–1012.
[29] B. Liu, C. Liu, X. Zou, D. Yan, J. Li, L. Jia, Proton uptake and proton distribution in perovskite materials for protonic ceramic fuel cell applications, Russ. Chem. Rev. 91 (11) (2022) RCR5063.
[30] H. Ding, W. Wu, C. Jiang, Y. Ding, W. Bian, B. Hu, P. Singh, C.J. Orme, L. Wang, Y. Zhang, D. Ding, Self-sustainable protonic ceramic electrochemical cells using a triple conducting electrode for hydrogen and power production, Nat. Commun. 11 (1) (2020) 1907.
[31] X. Xi, J. Liu, Y. Fan, L. Wang, J. Li, M. Li, J.L. Luo, X.Z. Fu, Reducing d-p band coupling to enhance CO_2 electrocatalytic activity by Mg-doping in $Sr_2FeMoO_{6-\delta}$ double perovskite for high performance solid oxide electrolysis cells, Nano Energy 82 (2021).
[32] B. He, L. Zhao, S. Song, T. Liu, F. Chen, C. Xia, $Sr_2Fe_{1.5}Mo_{0.5}O_{6-\delta}$- $Sm_{0.2}Ce_{0.8}O_{1.9}$ composite anodes for intermediate-temperature solid oxide fuel cells, J. Electrochem. Soc. 159 (5) (2012) B619–B626.
[33] Z. Du, H. Zhao, S. Yi, Q. Xia, Y. Gong, Y. Zhang, X. Cheng, Y. Li, L. Gu, K. Swierczek, High-performance anode material $Sr_2FeMo_{0.65}Ni_{0.35}O_{6-\delta}$ with in situ exsolved nanoparticle catalyst, ACS Nano 10 (9) (2016) 8660–8669.
[34] Y. Wang, T. Liu, M. Li, C. Xia, B. Zhou, F. Chen, Exsolved Fe–Ni nano-particles from $Sr_2Fe_{1.3}Ni_{0.2}Mo_{0.5}O_6$ perovskite oxide as a cathode for solid oxide steam electrolysis cells, J. Mater. Chem. 4 (37) (2016) 14163–14169.
[35] P. Qiu, X. Yang, W. Wang, T. Wei, Y. Lu, J. Lin, Z. Yuan, L. Jia, J. Li, F. Chen, Redox-reversible electrode material for direct hydrocarbon solid oxide fuel cells, ACS Appl. Mater. Interfaces 12 (12) (2020) 13988–13995.
[36] X. Xi, X.W. Wang, Y. Fan, Q. Wang, Y. Lu, J. Li, L. Shao, J.L. Luo, X.Z. Fu, Efficient bifunctional electrocatalysts for solid oxide cells based on the structural evolution

of perovskites with abundant defects and exsolved CoFe nanoparticles, J. Power Sources 482 (2021), 228981.
[37] T. Zheng, C. Liu, C. Guo, M. Zhang, X. Li, Q. Jiang, W. Xue, H. Li, A. Li, C.W. Pao, J. Xiao, C. Xia, J. Zeng, Copper-catalysed exclusive CO_2 to pure formic acid conversion via single-atom alloying, Nat. Nanotechnol. 16 (12) (2021) 1386–1393.
[38] J. Snyder, T. Fujita, M.W. Chen, J. Erlebacher, Oxygen reduction in nanoporous metal-ionic liquid composite electrocatalysts, Nat. Mater. 9 (11) (2010) 904–907.
[39] G. Barati Darband, M. Aliofkhazraei, A.S. Rouhaghdam, Facile electrodeposition of ternary Ni–Fe–Co alloy nanostructure as a binder free, cost-effective and durable electrocatalyst for high-performance overall water splitting, J. Colloid Interface Sci. 547 (2019) 407–420.
[40] S. Joo, K. Kim, O. Kwon, J. Oh, H.J. Kim, L. Zhang, J. Zhou, J.Q. Wang, H.Y. Jeong, J.W. Han, G. Kim, Enhancing thermocatalytic activities by upshifting the d-band center of exsolved Co–Ni–Fe ternary alloy nanoparticles for the dry reforming of methane, Angew. Chem., Int. Ed. Engl. 60 (29) (2021) 15912–15919.
[41] Y. Fan, X. Xi, D. Medvedev, Q. Wang, J. Li, J.L. Luo, X.Z. Fu, Emerging anode materials architectured with NiCoFe ternary alloy nanoparticles for ethane-fueled protonic ceramic fuel cells, J. Power Sources 515 (2021), 230634.
[42] B. Hammer, J.K. Nørskov, Theoretical surface science and catalysis—Calculations and concepts, Adv. Catal. 45 (2000) 71–129.
[43] B. Hammer, J.K. Norskov, Electronic factors determining the reactivity of metal surfaces, Surf. Sci. 343 (1995) 211–220.
[44] M. Mavrikakis, B. Hammer, J.K. Nørskov, Effect of strain on the reactivity of metal surfaces, Phys. Rev. Lett. 81 (1998) 2819–2822.
[45] J.R. Kitchin, J.K. Norskov, M.A. Barteau, J.G. Chen, Modification of the surface electronic and chemical properties of Pt(111) by subsurface 3d transition metals, J. Chem. Phys. 120 (21) (2004) 10240–10246.
[46] J.R. Kitchin, J.K. Norskov, M.A. Barteau, J.G. Chen, Role of strain and ligand effects in the modification of the electronic and chemical properties of bimetallic surfaces, Phys. Rev. Lett. 93 (15) (2004), 156801.
[47] J.K. Nørskov, F. Studt, F. Abild-Pedersen, T. bligaard, Fundamental Concepts in Heterogeneous Catalysis, 2014, pp. 117–119. New Jersey.
[48] J. Rager, M. Zipperle, A. Sharma, J.L. MacManus-Driscoll, Oxygen stoichiometry in Sr_2FeMoO_6, the determination of Fe and Mo Valence States, and the chemical phase diagram of SrO-Fe_3O_4-MoO_3, J. Am. Ceram. Soc. 87 (7) (2004) 1330–1335.
[49] D. Xiong, S.A. Rasaki, Y. Li, L. Fan, C. Liu, Z. Chen, Enhanced cathodic activity by tantalum inclusion at B-site of $La_{0.6}Sr_{0.4}Co_{0.4}Fe_{0.6}O_3$ based on structural property tailored via camphor-assisted solid-state reaction, J. Adv. Ceram. 11 (8) (2022) 1330–1342.
[50] D. Muñoz-Gil, D. Pérez-Coll, E. Urones-Garrote, U. Amador, S. García-Martín, Influence of the synthesis conditions on the crystal structure and properties of $GdBaCo_{2-x}Fe_xO_{5+\delta}$ oxides as air-electrodes for intermediate temperature solid oxide fuel cells, J. Mater. Chem. 5 (24) (2017) 12550–12556.
[51] Y. Xu, S. Yu, Y. Yin, L. Bi, Taking advantage of Li-evaporation in $LiCoO_2$ as cathode for proton-conducting solid oxide fuel cells, J. Adv. Ceram. 11 (12) (2022) 1849–1859.
[52] H.A. Shabri, M.H.D. Othman, M.A. Mohamed, T.A. Kurniawan, S.M. Jamil, Recent progress in metal-ceramic anode of solid oxide fuel cell for direct hydrocarbon fuel utilization: A review, Fuel Process, Technol. 212 (2021), 106626.
[53] Z. Teng, Z. Xiao, G. Yang, L. Guo, X. Yang, R. Ran, W. Wang, W. Zhou, Z. Shao, Efficient water splitting through solid oxide electrolysis cells with a new hydrogen electrode derived from A-site cation-deficient $La_{0.4}Sr_{0.55}Co_{0.2}Fe_{0.6}Nb_{0.2}O_{3-\delta}$ perovskite, Mater, Today Energy 17 (2020), 100458.
[54] X. Xi, J. Liu, W. Luo, Y. Fan, J. Zhang, J.L. Luo, X.Z. Fu, Unraveling the enhanced kinetics of $Sr_2Fe_{1+x}Mo_{1-x}O_{6-\delta}$ electrocatalysts for high-performance solid oxide cells, Adv. Energy Mater. 11 (48) (2021), 2102845.
[55] H. Lv, T. Liu, X. Zhang, Y. Song, H. Matsumoto, N. Ta, C. Zeng, G. Wang, X. Bao, Atomic-scale insight into exsolution of CoFe alloy nanoparticles in $La_{0.4}Sr_{0.6}Co_{0.2}Fe_{0.7}Mo_{0.1}O_{3-\delta}$ with efficient CO_2 electrolysis, Angew. Chem., Int. Ed. Engl. 59 (37) (2020) 15968–15973.
[56] S. Park, Y. Kim, Y. Noh, T. Kim, H. Han, W. Yoon, J. Choi, S.H. Yi, W.J. Lee, W.B. Kim, A sulfur-tolerant cathode catalyst fabricated with in situ exsolved CoNi alloy nanoparticles anchored on a Ruddlesden–Popper support for CO_2 electrolysis, J. Mater. Chem. 8 (1) (2020) 138–148.
[57] H. Lv, L. Lin, X. Zhang, D. Gao, Y. Song, Y. Zhou, Q. Liu, G. Wang, X. Bao, In situ exsolved $FeNi_3$ nanoparticles on nickel doped $Sr_2Fe_{1.5}Mo_{0.5}O_{6-\delta}$ perovskite for efficient electrochemical CO_2 reduction reaction, J. Mater. Chem. 7 (19) (2019) 11967–11975.
[58] Y.Q. Zhang, J.H. Li, Y.F. Sun, B. Hua, J.L. Luo, Highly active and redox-stable Ce-doped LaSrCrFeO-based cathode catalyst for CO_2 SOECs, ACS Appl. Mater. Interfaces 8 (10) (2016) 6457–6463.
[59] F. Ciucci, C. Chen, Analysis of electrochemical impedance spectroscopy data using the distribution of relaxation times: A bayesian and hierarchical bayesian approach, Electrochim. Acta 167 (2015) 439–454.
[60] T.H. Wan, M. Saccoccio, C. Chen, F. Ciucci, Influence of the discretization methods on the distribution of relaxation times deconvolution: Implementing radial basis functions with DRTtools, Electrochim. Acta 184 (2015) 483–499.
[61] A. Hauch, M. Marchese, A. Lanzini, C. Graves, Re-activation of degraded nickel cermet anodes-nano-particle formation via reverse current pulses, J. Power Sources 377 (2018) 110–120.
[62] H.P. Dasari, S.Y. Park, J. Kim, J.H. Lee, B.K. Kim, H.J. Je, H.W. Lee, K.J. Yoon, Electrochemical characterization of Ni–yttria stabilized zirconia electrode for hydrogen production in solid oxide electrolysis cells, J. Power Sources 240 (2013) 721–728.
[63] A. Hauch, K. Brodersen, M. Chen, M.B. Mogensen, Ni/YSZ electrodes structures optimized for increased electrolysis performance and durability, Solid State Ionics 293 (2016) 27–36.
[64] X. Tong, S. Ovtar, K. Brodersen, P.V. Hendriksen, M. Chen, A 4x4 $cm^{(2)}$ nanoengineered solid oxide electrolysis cell for efficient and durable hydrogen production, ACS Appl. Mater. Interfaces 11 (29) (2019) 25996–26004.
[65] A. Kromp, H. Geisler, A. Weber, E. Ivers-Tiffée, Electrochemical impedance modeling of gas transport and reforming kinetics in reformate fueled solid oxide fuel cell anodes, Electrochim. Acta 106 (2013) 418–424.
[66] T. Zhu, H. Troiani, L.V. Mogni, M. Santaya, M. Han, S.A. Barnett, Exsolution and electrochemistry in perovskite solid oxide fuel cell anodes: Role of stoichiometry in $Sr(Ti,Fe,Ni)O_3$, J. Power Sources 439 (2019), 227077.
[67] Y. Gao, J. Wang, Y.Q. Lyu, K. Lam, F. Ciucci, In situ growth of Pt_3Ni nanoparticles on an A-site deficient perovskite with enhanced activity for the oxygen reduction reaction, J. Mater. Chem. 5 (14) (2017) 6399–6404.
[68] Y.F. Sun, J.H. Li, L. Cui, B. Hua, S.H. Cui, J. Li, J.L. Luo, A-site-deficiency facilitated in situ growth of bimetallic Ni–Fe nano-alloys: A novel coking-tolerant fuel cell anode catalyst, Nanoscale 7 (25) (2015) 11173–11181.
[69] H. Kim, C. Lim, O. Kwon, J. Oh, M.T. Curnan, H.Y. Jeong, S. Choi, J.W. Han, G. Kim, Unveiling the key factor for the phase reconstruction and exsolved metallic particle distribution in perovskites, Nat. Commun. 12 (1) (2021) 6814.
[70] G. Kresse, J. Furthmüller, Efficiency of ab-initio total energy calculations for metals and semiconductors using a plane-wave basis set, Comput. Mater. Sci. 6 (1) (1996) 15–50.
[71] J.P. Perdew, K. Burke, M. Ernzerhof, Generalized gradient approximation made simple, Phys. Rev. Lett. 77 (18) (1996) 3865–3868.

Cheng Li is a Master degree candidate in School of Materials Science and Engineering, Huazhong University of Science and Technology. He received his B.S. in Materials Science and Engineering from Huaqiao University in 2018. Now he is working on electrode materials of O-type solid oxide cells (SOCs) and seawater electrolysis utilization.

Jian Li is a Professor in School of Materials Science and Engineering at Huazhong University of Science and Technology. He received his PhD in Metallic Materials from Central Iron & Steel Research Institute in 1988, and in Ceramic Engineering from the University of Illinois at Urbana-Champaign in 1995. He joined Huazhong University of Science and Technology and led the Center for Fuel Cell Innovation to develop materials, single cells, stacks and power system of solid oxide fuel cell.

Lichao Jia received his PhD in Materials Science from Huazhong University of Science and Technology in 2012. Then he worked with Prof. Jian Li at Huazhong University of Science and Technology as a postdoctoral fellow until 2014, during this period he visited Curtin University, Australia and worked with Prof. San Ping Jiang for 1 year as a visiting scholar. Currently he is a Professor in School of Materials Science and Engineering at Huazhong University of Science and Technology. His research interests are development of high-performance electrodes for SOFC and SOEC, combining theoretical and experimental studies.